Asymmetrically Coordinated CoB$_1$N$_3$ Moieties for Selective Generation of High-Valence Co-Oxo Species via Coupled Electron–Proton Transfer in Fenton-like Reactions

Junsheng Song, Nannan Hou,* Xiaocheng Liu, Markus Antonietti, Pengjun Zhang, Rongrong Ding, Li Song, Yang Wang,* and Yang Mu*

High-valence metal species generated in peroxymonosulfate (PMS)-based Fenton-like processes are promising candidates for selective degradation of contaminants in water, the formation of which necessitates the cleavage of O–H and O–O bonds as well as efficient electron transfer. However, the high dissociation energy of O–H bond makes its cleavage quite challenging, largely hampering the selective generation of reactive oxygen species. Herein, an asymmetrical configuration characterized by a single cobalt atom coordinated with boron and nitrogen (CoB$_1$N$_3$) is established to offer a strong local electric field, upon which the cleavage of O–H bond is thermodynamically favored via a promoted coupled electron–proton transfer process, which serves an essential step to further allow O–O bond cleavage and efficient electron transfer. Accordingly, the selective formation of Co(IV)=O in a single-atom Co/PMS system enables highly efficient removal performance toward various organic pollutants. The proposed strategy also holds true in other heteroatom doping systems to configure asymmetric coordination, thus paving alternative pathways for specific reactive species conversion by rationalized design of catalysts at atomic level toward environmental applications and more.

J. Song, N. Hou, X. Liu, R. Ding, Y. Mu
CAS Key Laboratory of Urban Pollutant Conversion
Department of Environmental Science and Engineering
University of Science & Technology of China
Hefei, Anhui 230026, P. R. China
E-mail: hounan@ustc.edu.cn; yangmu@ustc.edu.cn
M. Antonietti, Y. Wang
Department of Colloid Chemistry
Max Planck Institute of Colloids and Interfaces
14476 Potsdam, Germany
E-mail: yang.wang@mpikg.mpg.de
P. Zhang, L. Song
CAS Center for Excellence in Nanoscience
National Synchrotron Radiation Laboratory
University of Science & Technology of China
Hefei, Anhui 230029, P. R. China

1. Introduction

The peroxymonosulfate (PMS) activation process lies at the frontier to degrade various contaminants and alleviate the water pollution crisis, and single-atom catalysts (SACs) have received wide attention in it.[1] Typically, atomically dispersed cobalt (Co) atoms anchored on nitrogen-doped carbon substrates are emerging as model catalysts due to their high reactivity and low cost.[2] Free radicals (SO$_4^{\bullet-}$/HO•) with strong oxidizing ability are widely recognized as reactive species in SA-Co/PMS systems,[3] they are however prone to be consumed by the coexisting substrates and unfavorable for selective degradation of pollutants.[4] Therefore, unorthodox high-valence Co-Oxo species (i.e., Co(IV)=O) are in the focus, due to the combined merits of appreciable oxidizing ability, higher steady-state concentration, longer lifetime, and excellent anti-interference properties.[5,6] The conversion from Co(II) to Co(IV)=O with the concomitant production of SO$_4^{2-}$ and H$^+$ generally proceeds via O–H and O–O bonds cleavage in Co(II)-PMS complex, coupled with a two-electron transfer process.[6] However, due to the high bond dissociation energy of O–H,[7] the transformation of PMS tends to produce SO$_4^{\bullet-}$/HO• by direct cleavage of O–O bond through strong interaction with the heterogeneous SA-Co catalyst. Despite the substantial progress in the formation of high-valence metal species over a large library of SAC systems (e.g., Co, Fe, and Cu) during PMS activation, O–O bond cleavage and electron transfer are dominating pathways,[4,8] leaving the O–H bond cleavage as an essential step unavailable. In this regard, alternative strategies to facilitate O–H bond cleavage are crucial for the selective formation of Co(IV)=O and highly-efficient pollutant removal.

Coupled electron–proton transfer (CEPT), characterized by a concerted elementary step of proton and electron transfer, refers to a nonclassical redox process in which the proton and electron can transfer in two separate acceptors.[9] In this way, the bond dissociation energy falls in a more variable range,[10] which offers possibility to achieve thermodynamically favored O–H bond cleavage. Also, the proton-transfer process in CEPT can downshift the kinetic energy barrier by optimizing local geometries

**ADVANCED
SCIENCE NEWS**

www.advancedsciencenews.com

**ADVANCED
MATERIALS**

www.advmat.de

of catalysts.[11] Therefore, regulating the coordination configurations of single Co atoms to promote CEPT in the Co(II)-PMS complex would be highly desirable for the formation of high-valence Co-Oxo species in SA-Co catalysts.

External electric field may polarize the polar O–H bond in PMS and facilitate its cleavage, such an efficient trigger has already been verified for O–H bond dissociation of water molecules in hydrogen evolution reactions.[12] Therefore, heterogeneous SA-Co catalysts with a strong built-in electric gradient surrounding the coordination sites may boost the CEPT from the O–H bond during PMS activation. Note that the traditional symmetric CoN_4 configuration finds its efficacy in the generation of $SO_4^{\bullet-}/HO\bullet$ but fails to activate O–H bond, as the local electric field is quite weak for symmetry reasons. Construction of an asymmetric coordination microenvironment with high polarity is seemingly plausible for the generation of a stronger external electric field. Ideally, non-metallic heteroatom doping (e.g., sulfur, phosphorous, and boron) is promising to reshape the local environment of the carbon-based substrates to afford strong polarity.[13] Due to the similarity in atomic radius and the large difference in electronegativity between boron (B) and nitrogen (N), B tends to partially replace N atoms in covalent substrate and directly coordinates with Co, while the altered configuration comes with larger electric field contributions. The resulting asymmetric structure is then expected to facilitate proton transfer with minimized energy barriers, and finally to boost a catalytic cycle based on high-valence Co-Oxo species.

In this work, we successfully established a covalent matrix supported by CoB_1N_3 single-atom configuration as a proof-of-concept. The catalytic system shows high removal efficiency toward various organic pollutants via selectively generated high-valence Co-Oxo species (Co(IV)=O). Specifically, sulfamethoxazole (SMX) could be completely removed within 15 seconds in CoB_1N_3/PMS system with a pseudo-first-Order kinetic constant (k) reaching high up to 0.30 s^{-1}, 9.1 times higher than that of the traditional CoN_4/PMS system. Enabled by in situ Raman, synchrotron-radiation-based Fourier-transform infrared (SR FTIR) spectra and density functional theory (DFT) calculations, we found that during the first step of PMS adsorption on CoB_1N_3 moiety, a barrier-free intramolecular proton transfer from O–H to the edge O atom in PMS, coupled with strong electron transfer between Co and adsorbed O, is activated under the local electric field. The CEPT process further contributes to rapid conversion to high-valence Co-Oxo species for subsequent catalytic reaction. These findings provide a reference for the design of Fenton-like catalysts with high activity and selectivity. Furthermore, the CEPT mechanism highlights the exciting pathways to explain the formation of other high-valence metal species, such as Mn, Fe, Cu, etc.

2. Results and Discussion

The B-doped single-atom Co catalyst (termed as Co_{SA}-BNC, NC denotes N-doped carbon) was prepared by using chitosan, boric acid, and cobalt dichloride as precursors, followed by segmental pyrolysis under vacuum and then 20% H_2/Ar atmosphere. Meanwhile, Co_{SA}-NC was fabricated as a reference sample by calcining the mixture of chitosan and cobalt dichloride under a vacuum (**Figure 1**a). The Co contents of Co_{SA}-NC and Co_{SA}-BNC,

determined by inductively coupled plasma optical emission spectroscopy (ICP-OES), are 1.5 and 0.8 wt.%, respectively (Table S1, Supporting Information). Besides, B doping promotes the formation of carbon defects, as revealed by the higher I_D/I_G values of Co_{SA}-BNC and BNC relative to Co_{SA}-NC and NC (Figure S1, Supporting Information). Moreover, B doping endows Co_{SA}-BNC with improved hydrophilicity (Figure S2, Supporting Information) and larger surface area (Table S1, Supporting Information), which exposes more active sites for catalytic reactions.

X-ray diffraction (XRD) patterns were first recorded to roughly evaluate the dispersion status of Co in the Co_{SA}-BNC and Co_{SA}-NC (Figure 1b). Note that Co nanoparticles were co-formed after pyrolysis (termed as Co_{NPs}-NC), which were removed (Co_{SA}-NC) after acid leaching treatment, the resultant Co_{SA}-NC is then characterized by amorphous structure (Figure S3a,b, Supporting Information). In contrast, Co_{SA}-BNC exhibits a peak-free diffraction pattern without acid treatment (Figure 1b), and the highly dispersed Co species are also confirmed by the transmission electron microscopy (TEM) images (Figure S3c, Supporting Information), which suggests that B doping promotes the atomic-level dispersion of Co. The aberration-corrected high-angle annular dark-field scanning transmission electron microscopy (AC-HAADF-STEM) images (Figure 1c,d; Figure S3d,e, Supporting Information) verify that Co atoms are atomically isolated on the covalent substrate in both Co_{SA}-NC and Co_{SA}-BNC. In addition, C, N, B, and Co atoms are distributed uniformly throughout the Co_{SA}-BNC catalyst, as evidenced by the energy-dispersive X-ray spectroscopy (EDS) mapping images (Figure 1e). These results collectively point to the formation of single Co atoms in Co_{SA}-BNC and Co_{SA}-NC.

To further explore the electronic structure and coordination environments of single Co atoms in Co_{SA}-BNC and Co_{SA}-NC, soft X-ray absorption spectroscopy (XAS), hard XAS, and X-ray photoelectron spectroscopy (XPS) were performed. X-ray absorption near edge structure (XANES) of Co K-edge spectra reveal an increased electropositivity of Co after B doping, although the valence states of both Co_{SA}-NC and Co_{SA}-BNC are close to +2 after hydrogen treatment (**Figure 2**a; Figure S4, Supporting Information). Compared to Co_{SA}-NC, the decreased intensity of pre-edge peak and increased intensity of white-line peak in Co_{SA}-BNC suggest the reduced symmetry and rearranged charge polarization,[14] demonstrating the altered coordination environment of Co atoms upon B doping. The extended X-ray absorption fine structure (EXAFS) spectra indicated the absence of a peak assigned to Co–Co bond (2.17 Å) in R space,[15] further verifying the atomic dispersion of Co (Figure 2b). This is also in line with the wavelet transform (WT)-EXAFS results (Figure 2c), in which the maximum intensity observed in Co_{SA}-BNC and Co_{SA}-NC is clearly separated from the plots of Co foil which is mainly located at 7.5 Å^{-1} (Co–Co bond).[15] Also, the center of Co_{SA}-BNC shows a slight negative shift compared to that of Co_{SA}-NC (Figure 2c), suggesting that the Co atoms in Co_{SA}-BNC might coordinate with foreign atoms with a smaller atomic number than N or C, which is assigned to B atoms in our case. Next, we identified the coordination structure of Co_{SA}-NC as symmetrical CoN_4. As shown in the N K-edge spectrum of Co_{SA}-NC (Figure S5, Supporting Information), Co atoms are coordinated with pyridinic N,[16] and the Co–N coordination number in Co_{SA}-NC is determined to be 4.1 based on the fitting results of EXAFS curve (Figure S6
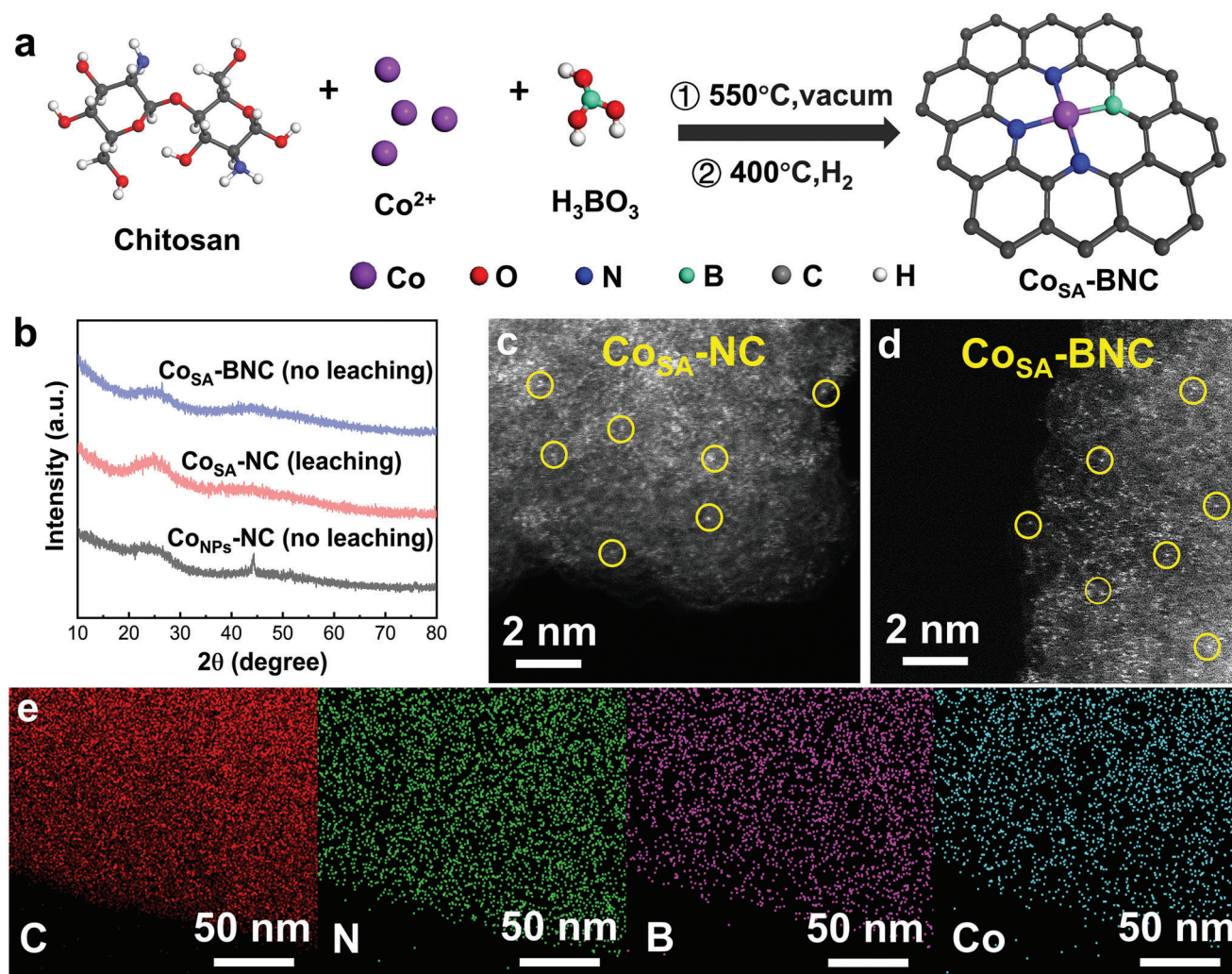
Figure 1. a) Formation process of Co$_{SA}$-BNC. b) XRD patterns of synthesized samples. Co$_{SA}$-BNC was synthesized without an acid leaching step, while the formation of Co$_{SA}$-NC requires acid treatment, otherwise, the product is identified as Co$_{NPs}$-NC, c,d) AC-HAADF-STEM images of Co$_{SA}$-NC (c) and Co$_{SA}$-BNC (d). e) EDS mapping results of Co$_{SA}$-BNC.

and Table S2, Supporting Information), demonstrating the successful preparation of traditional CoN$_4$ as a reference sample. We then tried to probe the interplay between Co and B/N in Co$_{SA}$-BNC. The N K-edge XANES spectrum in Figure 2d reveals the formation of Co-pyridinic N bond. The L-edge position of Co$_{SA}$-BNC falls between that of Co$_{SA}$-NC and CoB (Figure 2e), implying the formation of Co–B besides Co–N bond, as further verified by the B 1s XPS spectrum, in which the peak at 186.8 eV is associated with Co–B interaction (Figure 2f).[17] Meanwhile, the peaks located at 288.0 and 289.1 eV in the C K-edge spectrum also suggest the formation of C–N and C–B bonds in Co$_{SA}$-BNC (Figure S7, Supporting Information).[16b,18] The combined results reveal the coexistence of Co–B–C and Co–N–C. Serving as the anchoring sites for single Co atoms, the pyridinic N and newly incorporated B can explain the promoted single atom isolation after B doping, which is directly formed without acid leaching treatment. Considering that the oxygen(O)-rich chitosan may share coordination sites with Co atoms in the synthesized Co$_{SA}$-BNC, we recorded Co 2p and O 1s XPS spectra and found no signals

assigned to Co–O bonding (Figure S8, Supporting Information). Quantitatively, we simulated the EXAFS (Figure 2g; Table S2) spectra of Co$_{SA}$-BNC and found that the coordination numbers of Co–N and Co–B were 3.3 and 1.3, respectively, suggesting the asymmetric CoB$_1$N$_3$ moiety is preferred. We also checked the rationality of CoB$_1$N$_3$ as the main configuration by DFT calculations (Figure S9, Supporting Information). Specifically, we investigated the possibility to anchor a Co atom onto different B, N co-doped carbon substrates (B$_x$N$_{4-x}$, x = 1, 2, 3). The estimated binding energies of atomic Co with B$_1$N$_3$-, B$_2$N$_2$-, and B$_3$N$_1$-carbon are −5.5, −4.8, and −4.6 eV, respectively. The highest binding energy clearly indicates the dominant configuration of CoB$_1$N$_3$ among the three reasonable structures. To obtain a comprehensive understanding of the local geometrical structure, we further conducted the XAENS spectra simulation of CoN$_3$B$_1$ and CoN$_4$ configurations (Figure S10, Supporting Information). The simulated XANES spectrum of CoN$_3$B$_1$ matches well with the experimental one, which further confirms the main component of Co$_{SA}$-BNC. In comparison, the simulated XANES spectra of CoN$_3$B$_1$
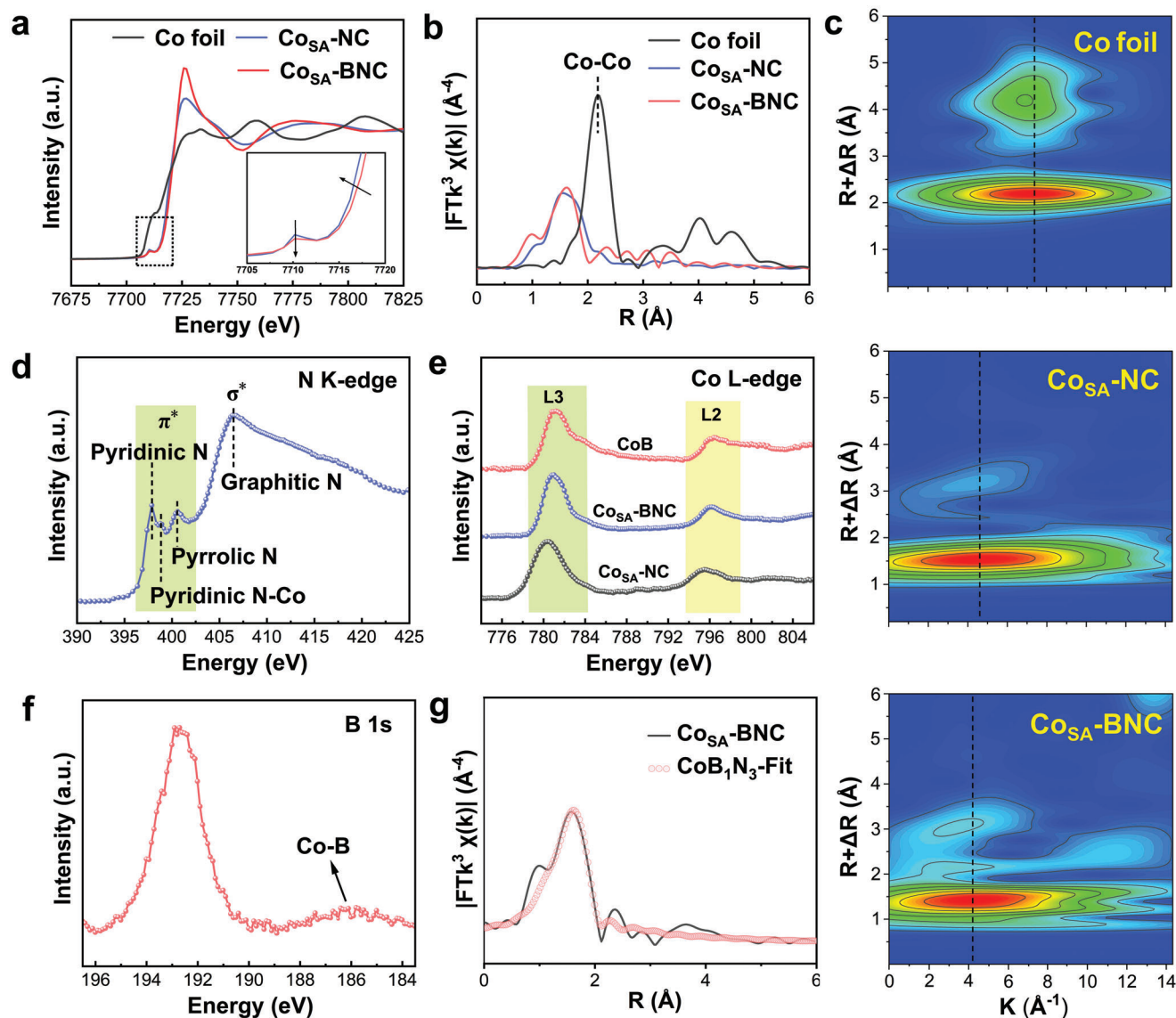
Figure 2. a) Co K-edge XANES spectra, b) FT k^3-weighted Co K-edge EXAFS spectra, and c) WT-EXAFS plots of Co_{SA}-BNC and the reference samples (Co foil and Co_{SA}-NC). d) N K-edge soft XAS spectrum of the Co_{SA}-BNC. e) Co L-edge soft XAS spectra of Co_{SA}-BNC, Co_{SA}-NC, and CoB. f) B 1s XPS spectrum of Co_{SA}-BNC. g) FT-EXAFS fitting curves of Co_{SA}-BNC at Co K-edge.

and CoN_4 exhibit similar tendencies in terms of the difference in white-line peak intensity (Figure S10c, Supporting Information), keeping consistent with the experimental results. The combined results confirm the formation of symmetric CoN_4 in Co_{SA}-NC and heteroatom-substituted asymmetric CoB_1N_3 in Co_{SA}-BNC.

SMX was initially selected to evaluate the catalytic performance of Co_{SA}-BNC and Co_{SA}-NC in PMS activation process. The adsorption rates of NC, BNC, Co_{SA}-NC, and Co_{SA}-BNC on SMX are all <5%, their contribution to the degradation results can be neglected (Figures S11 and S12, Supporting Information). Impressively, SMX could be completely removed within 15 s in Co_{SA}-BNC/PMS system with a k value of 0.30 s^{-1}, which is 9.1 times higher than that of Co_{SA}-NC (**Figure 3**a). Besides, CoB_1N_3 exhibits excellent structural integrity and recycling performance in PMS activation (Figures S13 and S14, Supporting Informa-

tion), which could remove 92.2% of SMX even in the fourth cycle (Figure S14, Supporting Information). Electron spin resonance (EPR) tests were conducted to probe the potential reactive species such as •OH, $SO_4^{•-}$ or $^1O_2$ (Figure S15, Supporting Information), as widely reported in PMS activation process. The concentrations of •OH and $SO_4^{•-}$ in Co_{SA}-BNC are slightly lower than that in Co_{SA}-NC, matching well with the probe experiments using benzoic acid (BA) as a probe molecule (Figure S16, Supporting Information). On the other hand, there is negligible $^1O_2$ generation in the two systems (Figure S17, Supporting Information). Quenching experiments show that the SMX degradation efficiency only decreases to 81% ($k = 0.20$ s^{-1}) and 89% ($k = 0.29$ s^{-1}) when methanol (MeOH, radical scavenger for $SO_4^{•-}$ and •OH) or *tert*-Butanol (TBA, radical scavenger for •OH) is added, respectively. Therefore, these free radicals are not dominant

ADVANCED
SCIENCE NEWS
www.advancedsciencenews.com
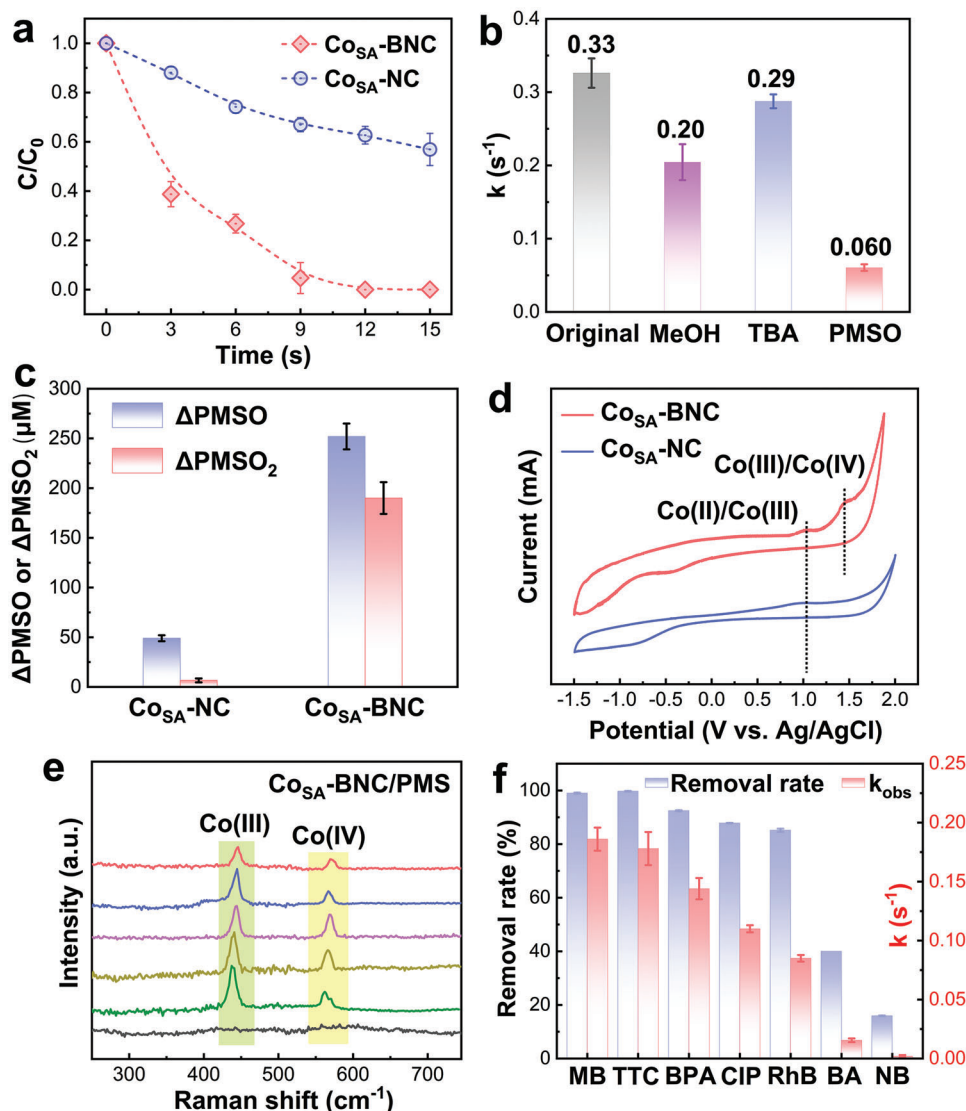
ADVANCED
MATERIALS
www.advmat.de

Figure 3. a) SMX degradation profiles of Co_{SA}-BNC and Co_{SA}-NC, catalyst dosage = 0.01 g L^{-1}, error bars represent the standard deviations from 10 independent measurements. b) Comparison of quenching kinetics under different conditions (all data were from the same batch). c) PMSO consumption and PMSO$_2$ generation in the two catalytic systems, [PMSO]$_0$ = 2 mM, sampling time = 15 s. d) CV curves of Co_{SA}-BNC and Co_{SA}-NC in the mixed solution of Na$_2$SO$_4$ (50 mM) and PMS (2 mM). e) In situ Raman spectra of Co_{SA}-BNC/PMS under a 633 nм laser ([PMS]$_0$ = 4 mM), the test interval was two minutes from the bottom up. f) Removal rates and corresponding k values of different organic contaminants in the Co_{SA}-BNC /PMS system, catalyst dosage = 0.1 g L^{-1}. General reaction conditions: [PMS]$_0$ = 0.8 mM (if not otherwise specified), [Pollutant]$_0$ = 45 μм, pH = 7, [TBA] = [MeOH] = 0.5 M, [PMSO] = 15 mM (if needed).

reactive oxygen species in Co_{SA}-BNC/PMS, although they constitute the main contributors in Co_{SA}-NC (Figure 3b; Figure S18, Supporting Information).[2a] This motivated us to explore the possible contribution from high-valence Co-Oxo species, which has been reported in homogenous Co^{2+} or heterogenous $CoCO_3$-catalyzed PMS activation processes.[5b,6] Herein, methyl phenyl sulfoxide (PMSO) was used to probe the existence of high-valence Co-Oxo species, as it readily turns to sulfone (PMSO$_2$) via oxygen transfer.[19] As expected, a much higher concentration of PMSO$_2$ is detected in Co_{SA}-BNC/PMS (Figure 3c; Figure S19, Supporting Information), demonstrating that Co_{SA}-BNC significantly promotes the formation of high-valence Co-Oxo species. The ^{18}O-isotope-labeled PMSO$_2$ ($C_7H_8^{16}O^{18}O$) is also detected in Co_{SA}-

BNC/PMS, which unambiguously verifies the presence of high-valence Co species (Figure S20, Supporting Information).[20] Accordingly, the degradation efficiency is remarkably reduced when PMSO is added (Figure 3b), highlighting the primary contribution from high-valence Co-Oxo species in pollutant removal.[8f] We also found that the consumed PMS is only 6.2% in the presence of bare PMSO (Figure S21, Supporting Information), this indicates that PMSO suppresses SMX degradation primarily by quenching the active species rather than consuming PMS. Moreover, cyclic voltammetry (CV) curves and in situ Raman spectra were collected, and the combined results keep consistent with those of PMSO probe experiments and quenching tests. Specifically, a distinct peak at 1.4–1.5 V assigned to Co(III)/Co(IV)

ADVANCED
SCIENCE NEWS
www.advancedsciencenews.com

ADVANCED
MATERIALS
www.advmat.de

oxidation process is detected in the CV curve of Co_{SA}-BNC/PMS system (Figure 3d), while the peak at ≈1.1 V in Co_{SA}-NC/PMS signifies the Co(II)/Co(III) oxidation process.[21] The higher electron-donating and catalytic ability of Co_{SA}-BNC enables O_2 or H^+ in solution (stemming from the dissociation of BS or PMS) to accept the electrons from the catalyst. The peak centered ≈ −0.6 V is then likely to relate with oxygen reduction or hydrogen evolution reaction,[22] which is however absent in Co_{SA}-NC with much lower activity. The valence transformation from Co(III) to Co(IV) is also tracked by the in situ Raman spectra of Co_{SA}-BNC/PMS. In addition to the generation and conversion of Co(III) located at 436 cm^{-1}, a signal assigned to Co(IV) at 578 cm^{-1} gradually increases (Figure 3e).[23] It is worth mentioning that the high catalytic performance at seconds scale (Figure 3a) does not contradict the in situ Raman signals occurring at minutes scale (Figure 3e, Experimental Section) because the latter is inherently limited by Raman testing conditions which only allows the minimum time interval of 2 min for signal collection to assure reasonable control. Relative to that of Co_{SA}-NC which generates radicals via a one-electron transfer process, Co_{SA}-BNC is found to transfer twice as many electrons as Co_{SA}-NC through the rotating disk electrode tests (Figure S22, Supporting Information), suggesting that Co_{SA}-BNC prefers to activate PMS via the two-electron transfer pathway. These findings directly support the formation of high-valence Co-Oxo species (Co(IV)=O) in Co_{SA}-BNC/PMS system. In summary, the combination of PMSO probe experiments, quenching tests, CV curves, and in situ Raman confirm that CoB_1N_3 configuration significantly promotes the generation of high-valence Co(IV)=O species in PMS activation process, which in turn substantially advances pollutant removal performance. The proposed strategy to break the symmetry of metal coordination environment also finds its universality in phosphorous-doped single-atom Co catalyst (termed as Co_{SA}-PNC) to selectively generate high-valence Co-Oxo species (Experimental Procedures in Figure S23, Tables S3 and S4, Supporting Information).

As a result of the degradation process oxidized by Co(IV)=O in Co_{SA}-BNC/PMS system, TOC removal efficiency of SMX reaches 58.9% with an extremely low catalyst dosage (0.01 g L^{-1}), which climbs to 87.7% and 93.1% when the dosage increases to 0.05 and 0.1 g L^{-1}, respectively, suggesting that Co_{SA}-BNC could achieve high-level water purification with proper catalyst dosage (Figures S24 and S25, Supporting Information). Due to the inherent strong oxidizing ability of high-valence Co species, oxygen transfer, aniline oxidation, N−S bond cleavage, polymerization, and a series of ring-cleavage processes can be achieved in the SMX oxidation process (Figures S26–S28, Supporting Information).[4,6] In our system, we also detected the oxidation product of olefins. For example, two carbons can be detached from TP116 ($C_4H_8N_2O_2$) by olefin oxidation to form TP106 ($C_2H_6N_2O_3$). Two and four carbons can be detached from TP502 ($C_{20}H_{18}N_6O_6S_2$) via ring-cleavage and olefin oxidation to form TP526 ($C_{18}H_{18}N_6O_9S_2$) and TP518 ($C_{16}H_{18}N_6O_{10}S_2$), respectively. The final mineralized products are assumed to be CO_2 and water, suggesting the potential application of high-valence Co species in the mineralization of organic pollutants. Depending on the differences in electron-losing ability of organic pollutants, Co_{SA}-BNC can also achieve selective removal toward various pollutants (Figure 3f; Figures S29 and S30, Tables S5–S7 (Sup-

porting Information), Experimental Section), including methylene blue (MB), sulfamethoxazole (TTC), bisphenol A (BPA), ciprofloxacin (CIP) and rhodamine B (RhB), benzoic acid (BA) and nitrobenzene (NB), suggesting its favorable practicability.

To study the intrinsic formation mechanism of high-valence Co-Oxo species, DFT calculations were carried out to explore the possible intermediates in the dynamic catalytic process. We initially proposed that single Co atoms could catalyze the adsorbed PMS, which then directly split into SO_4^{2-} and H^+ to generate Co(IV)=O,[19] but it turned out to be thermodynamically unfavorable (Figure S31, Supporting Information), implying that other intermediates might be involved for the formation of Co(IV)=O. To directly investigate the surface chemical evolution of single-atom Co sites during PMS activation process, in situ Raman spectra were collected in both CoB_1N_3 and CoN_4 systems. As depicted in **Figure 4**a, the peaks centered at 881, 978 and 1060 cm^{-1} in CoB_1N_3/PMS system can be assigned to the adsorbed PMS (HSO_5^-), SO_4^{2-} and HSO_4^-, respectively.[24] A sharp signal of PMS appeared at 2 min and then rapidly decreases, accompanied by continuous accumulation of SO_4^{2-} with prolonged reaction time, implying the rapid PMS activation process (Figures S32–S34, Supporting Information). Besides, a peak at 835 cm^{-1} stemmed from the adsorbed peroxo species is clearly observed during the activation process, which indicates the strong Co-PMS interactions.[4] Notably, a sharp signal of HSO_4^- rapidly appears at 4 minutes, which further intensifies and then weakens, suggesting that HSO_4^- might serve as a key intermediate in the process of Co(IV)=O formation. Comparatively, the signals of HSO_5^- and SO_4^{2-} only experienced a moderate increase in CoN_4/PMS system (Figure 4b), reflecting the weaker adsorption and activation of PMS. The signal of HSO_4^- remains invisible, signifying that HSO_4^- contributes little to the formation of free radicals. These results are further supported by the synchrotron radiation-based Fourier-transform infrared (SR FTIR) spectra (Figure 4c), the distinct peak assigned to HSO_4^- (centered at 1150 cm^{-1}) in CoB_1N_3/PMS is not detectable in CoN_4/PMS.[25]

Given that B doping alters the symmetry of conventional CoN_4 configuration, non-uniform distribution of electrons and enhanced local electric field in asymmetric CoB_1N_3 are expected to trigger the CEPT process, which can facilitate the hetero-cleavage of polar O−H bond. The dissociated proton is prone to be captured by the edge O atoms (depicted as an intramolecular proton-transfer process), leaving two electrons retained in the O 2p orbital. Consequently, they are coupled with the other two electrons from single-atom Co donor to form Co=O double bond, further contributing to O−O bond cleavage. As a result, Co(II) is successfully transformed into Co(IV)=O accompanied by generation of HSO_4^-, which gradually transforms into H^+ and SO_4^{2-} (path 1 in Figure 4d). We notice that the redox potential of Co(IV)/Co(II) is recognized to be higher than HSO_5^-/SO_4^{2-} (>1.88 V vs 1.82 V),[26] however, the overall potential of PMS for oxidizing Co(II) to Co(IV) depends on the integrated contribution from E(HSO_5^-/=O) and E(HSO_5^-/SO_4^{2-}) (Figure S35a, Supporting Information). Therefore, the extra potential E(HSO_5^-/=O) of PMS provides possibility to drive Co(II)/Co(IV) transformation. Although the transformation from Co(II) to Co(IV) is dominated by two-electron transfer, we are not committed to excluding the existence of intermediate states, such as Co(III) (Figure S35b, Supporting Information). Temperature-dependent
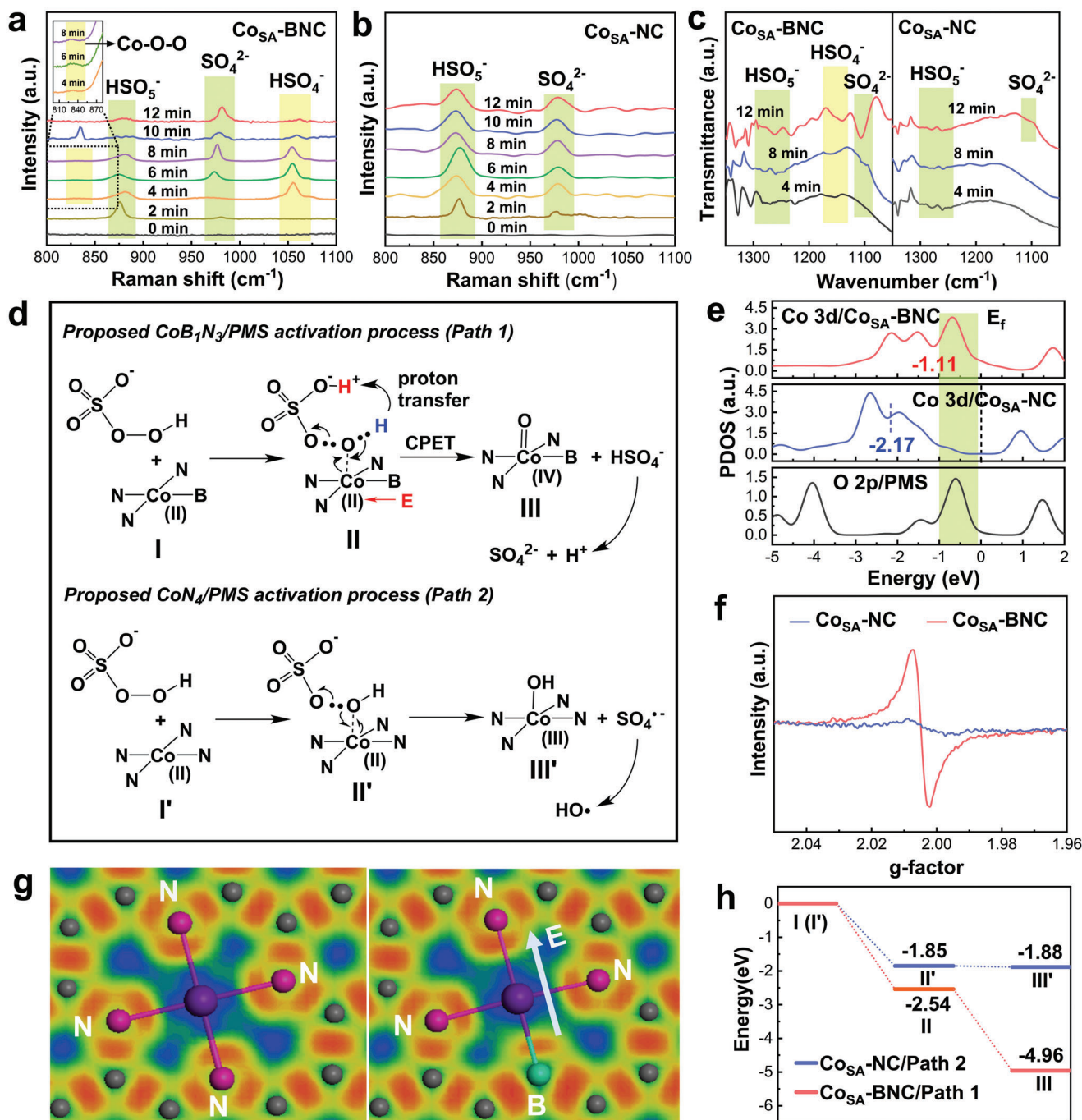
Figure 4. a,b) In situ Raman spectra of Co_{SA}-BNC/PMS (a) and Co_{SA}-NC/PMS (b) under a 532 nm laser, $[PMS]_0$ = 0.8 mM. c) SR FTIR spectra of the two systems. d) Proposed PMS activation pathways catalyzed by Co_{SA}-BNC (Path 1) and Co_{SA}-NC (Path 2). e) PDOS of Co 3d in CoB_1N_3, Co 3d in CoN_4 and absorbed O 2p in PMS. f) Low-temperature EPR test of Co_{SA}-NC and Co_{SA}-BNC. g) Electron localization function analysis of CoN_4 (left) and CoB_1N_3 (right). h) Energy profiles of PMS activation by the two configurations.

magnetization tests reveal that the single Co atoms in Co_{SA}-BNC possess a high spin state (Figure S35c, Supporting Information). Upon simulating the rearrangement of d-electrons with a square planar crystal field,[27] we found that the two most easily lost electrons are located in different energy levels (Figure S35d, Supporting Information), making them capable of losing in a suc-

cessive way. Due to O–H bond cleavage can take place when the two-electron transfer occurs between Co–O in CoB_1N_3/PMS, free radicals are not likely to be produced even when Co(III) intermediates exist. We also noted that path 1 is more favorable when the Co_{SA}-BNC/PMS system is situated in an alkaline solution, where the dissociated hydrogen can combine with OH^- to form

H_2O and accelerate the cleavage of O–H bond, further promoting the formation of Co(IV)=O by PMS activation and contributing to higher k value (Figures S36–S38, Supporting Information). On the other hand, PMS adsorbed on the single-atom Co sites in symmetric CoN_4 without a strong local electric field directly accepts one electron from single Co atoms to trigger O–O bond cleavage, which results in the generation of free radicals, without forming HSO_4^- (path 2 in Figure 4d).[28] The HSO_4^- detected by in situ Raman and SR-FTIR spectra indicates the intramolecular proton-transfer process in CoB_1N_3/PMS, and the coupled strong electron transfer is also revealed by open-circuit potential (OCP) measurements and projected density of states (PDOS) calculations (Figure 4e). The OCP of both CoN_4 and CoB_1N_3 systems increases when PMS is added, elucidating that single Co atoms donate electrons to PMS. The much higher kinetics and larger potential gap in CoB_1N_3/PMS arise from the greatly enhanced electron transfer, which is further confirmed by adding SMX and a more evident decrease of OCP (Figure S39, Supporting Information). Besides, PDOS calculations show that the single Co atoms in CoB_1N_3 possess a d-band center of −1.11 eV, which is much higher than that in CoN_4 (−2.17 eV), indicating the enhanced adsorption ability and better affinity to PMS.[29] In addition, the electrons of the Co 3d orbital in CoB_1N_3 are strongly overlapped with the adsorbed O 2p orbital in PMS, implying the intensified interaction and easier electron transfer between Co_{SA}-BNC and PMS, matching well with OCP tests. Collectively, the promoted CEPT process for the formation of Co(IV)=O in Co_{SA}-BNC/PMS is confirmed.

Low-temperature EPR spectra were recorded to evaluate the electronic state near central Co atoms. The signal intensity of CoB_1N_3 is dramatically strengthened relative to that of CoN_4, implying a higher concentration of free electrons (Figure 4f; Figure S40, Supporting Information). These unpaired electrons of single Co atoms in CoB_1N_3 are more likely to be attracted by the asymmetrically coordinated electron-withdrawing atoms with strong electronegativity, causing non-uniform distribution of electrons to create a local electric field. Electron localization function analysis was further conducted to simulate the electron distribution around central Co sites (Figure 4g). Obviously, the electrons of four pyridinic N atoms are uniformly distributed on a highly symmetrical CoN_4 configuration. However, loss of electrons appears near Co–B bond when one pyridinic N is replaced by one B atom to form asymmetric CoB_1N_3, due to the larger electronegativity of N than B (3.04 vs 2.04). As such, a local polar electric field is built along the B→Co→N direction, which is also a reflection of the tailored spin state of Co atoms after B doping (Figure S35a, Supporting Information). This field is interpreted as an external force to facilitate proton transfer from O–H bond to the edge O atom. Energy barrier calculations also highlight that the proton transfer could proceed in a barrier-free manner under the local electric field of CoB_1N_3 (Figure S41, Supporting Information). DFT calculations of the corresponding energy profiles about the intermediate structures in CoB_1N_3 and CoN_4 are depicted in Figure 4h, Figures S42 and S43 (Supporting Information). For CoN_4, free radicals are more likely to generate through path 2. However, the adsorption model with an intramolecular proton transfer to firstly break O–H bond is preferred in CoB_1N_3, followed by a more thermodynamically favored O–O cleavage to form Co(IV)=O. The maximum total energy released during the reaction on CoB_1N_3 sites is 4.96 eV, significantly larger than that of CoN_4 (1.88 eV), again signifying the much higher conversion potential to form high-valence Co(IV)=O in CoB_1N_3.

3. Conclusion

Our experimental results and theoretical analyses clearly demonstrated that the asymmetrical CoB_1N_3 configuration dramatically enhances the activation of PMS to selectively generate high-valence Co-Oxo species, which allows ultrafast removal efficiency toward various organic pollutants. The doping of B atoms induces a strong local electric field around the atomic Co, thus promoting the CEPT process during the first step of PMS adsorption, facilitating peroxy O–O bond cleavage in the conversion pathway to Co(IV)=O. This work highlights that the selective generation of high-valence metal species in Fenton-like reactions can be achieved through rational design of catalysts at atomic level. Moreover, the promoted CEPT enabled by local electric field in asymmetric configurations of the large SAC family, also provides exciting opportunities for the development of catalysts to cleave O–H bonds in organometallic and/or inorganometallic catalysis.

4. Experimental Section

Synthesis of Co_{SA}-BNC and Co_{SA}-NC: Chitosan (1 g), acetic acid (0.25 mL), $CoCl_2·6H_2O$ (60 mg), and H_3BO_3 (180 mg) were mixed in 50 mL deionized water by continuous stirring to obtain a homogeneous gel solution. Then, the mixture was spread in a petri dish (diameter: 10 cm) and dried at 60 °C under a vacuum for 24 h. The purple solid was heated to 550 °C with a ramping rate of 10 °C min⁻¹ and kept for 2 h under vacuum. Then, the product was ground into a fine powder and washed three times with 20 mL water and ethanol, respectively, followed by drying at 60 °C for 8 h. The powder was further mixed with 180 mg H_3BO_3 and ground thoroughly, followed by annealing under 400 °C for 2 h in H_2 (20% H_2/Ar) atmosphere. Finally, the powder was washed and dried with the same procedures as described above. The obtained dark powder was denoted as Co_{SA}-BNC. Similarly, 1 g chitosan, 0.25 mL acetic acid, 50 mL H_2O, and 60 mg $CoCl_2·6H_2O$ were mixed and dried, followed by pyrolysis at 550 °C for 2 h under vacuum. The product was denoted as Co_{NPs}-NC. Then, the product was leached in 0.25 M H_2SO_4 solution for 10 min. After washing with water and ethanol for three times and drying at 60 °C for 8 h, the obtained powder was denoted as Co_{SA}-NC.

Soft XAFS and hard XAFS Measurements: Soft XAS spectra were recorded at Beamlines MCD-A and MCD-B (Soochow Beamline for Energy Materials) in the National Synchrotron Radiation Laboratory (NSRL) in Hefei, China. Finally, the spectra were normalized to yield an edge jump to one. Hard XAFS spectra of Co K-edge were measured at the BL14W1 beamline stations in Shanghai Synchrotron Radiation Facility (SSRF) (Shanghai, China). Before the analysis at the beamline, samples were pressed into thin sheets (diameter: 1 cm) and sealed using Kapton tape film. The XAFS spectra were recorded at room temperature using a 4-channel Silicon Drift Detector (SDD) Bruker 5040. Using Si (311) double-crystal monochromator, the data collection was carried out in transmission mode at ambient conditions. The fitting details were shown in Supporting Information.

Measurements of Catalytic Performance: To evaluate the catalytic performance, catalysts were added into 50 mL of pollutant solution (45 μM), followed by the addition of 0.8 mM PMS. The pollutant solution was further added with 50 mM phosphate-buffered saline (PBS, 17.2 mM KH_2PO_4 mixed with 32.7 mM $Na_2HPO_4·12H_2O$) to maintain a stable pH value of 7. The sample was directly mixed with an equal volume of methanol and filtered with a filter membrane (Teflon, 0.22 μm) for further testing. To obtain reliable results in the catalytic reactions using Co_{SA}-BNC which could rapidly degrade pollutants, ten independent parallel experiments were

carried out to collect the data with error bars. The concentrations of SMX, BPA, BA, and NB were determined by ultra-performance liquid chromatography (UPLC, Agilent), while the concentrations of MB, RhB, TTC, and CIP were measured with a UV–vis spectrophotometer (U-3010, Hitachi) (details in Table S7). In the recycling test, the catalyst was filtrated after each run and rinsed thoroughly with pure water and ethanol for two times, respectively. After drying at 70 °C for 8 h under vacuum, the recovered catalyst was weighed and used in the next cycle.

Electrochemical Measurements: The electrochemical tests were conducted in a three-electrode system. A glassy carbon electrode loaded with catalysts, a platinum wire electrode, and an Ag/AgCl electrode were used as working electrodes, counter electrodes, and reference electrodes, respectively. First, 8 mg catalyst and 80 μL Nafion solution (5 wt.%) were dispersed in water/ethanol mixed solution (1 mL) under ultrasonication for 30 min. Then, the mixture (3 μL) was dropped three times onto the surface of polished glassy carbon electrode and dried at room temperature for 24 h. The scanning rate in CV tests was 200 mV s^{-1}.

Raman and SR FTIR Measurements: Raman analysis was carried out using a confocal microscopic Raman spectrometer (LabRam HR, Horiba, France). To evaluate the carbon defect of catalysts, a 532 nм laser was used and the ND filter was set to 5%. In the in situ Raman tests of the transformation of Co(III)/Co(IV), a 633 nм laser was used, and the ND filter was set as 25%. An in situ Raman test system was established using a purchased electrochemical in situ spectroscopy reaction cell (EC-RAIR–H). The catalyst (8 mg) was loaded onto glassy carbon with conductive adhesive and 20 mL of PMS solution was added until the liquid level was above the glassy carbon. The Raman laser was focused onto the surface of the catalyst through the solution layer, which could allow in situ detection of signal change on catalyst surface during the PMS activation reaction. Note that the laser should be refocused onto catalyst surface prior to next measurement, and a superimposed sampling process was necessary to afford a favorable signal-to-noise ratio. The duration time for a single scanning was 20 s and the controllable time interval for signal collection was set as 2 min. To test the chemical evolution of PMS on the surface of catalysts, a 532 nм laser was used, and the ND filter was set to 25%. The in situ synchrotron-radiation-based Fourier transform infrared (SR-FTIR) measurements were recorded between 4000 and 800 cm^{-1} at the Infrared Spectroscopy and Microspectroscopy Endstation (BL01B) at NSRL. In these measurements, catalysts mixed with 0.8 mм PMS solution were set in a glass slide covered with a ZnSe window.

DFT Calculations: First-principle calculations were conducted using density functional theory from CASTEP with a plane wave basis. The generalized gradient approximation (GGA) with spin-polarized Perdew–Burke–Ernzerhof (PBE) scheme was employed to calculate the exchange and correlation function. The core electrons were represented by the Vanderbilt-type ultrasoft pseudopotentials with Koelling–Harmon relativistic treatment. Energy cutoff was set as 450 eV and k-point was $2 \times 2 \times 1$.[30] The self-consistent field (SCF) tolerance and Max. force was converged to $< 1 \times 10^{-5}$ eV and <0.03 eV Å^{-1}, respectively. The Max. stress and Max. displacement were set as 0.05 GPa and 0.001 Å, respectively. DFT calculation of HOMO values was performed using the PBE generalized gradient approximation for the exchange-correlation function in the DMol3 code. The self-consistent field (SCF) tolerance converged to $<1 \times 10^{-6}$ eV. The Max. force and Max. displacement were set as 0.002 eV Å^{-1} and 0.005 Å, respectively.

Supporting Information

Supporting Information is available from the Wiley Online Library or from the author.

Acknowledgements

Conflict of Interest

The authors declare no conflict of interest.

Data Availability Statement

The data that support the findings of this study are available from the corresponding author upon reasonable request.

Keywords

[1] a) J. Lee, U. Gunten, J. H. Kim, *Environ. Sci. Technol.* **2020**, *54*, 3064; b) Y. Shang, X. Xu, B. Gao, S. Wang, X. Duan, *Chem. Soc. Rev.* **2021**, *50*, 5281; c) N. Zhang, C. Ye, H. Yan, L. Li, H. He, D. Wang, Y. Li, *Nano Res.* **2020**, *13*, 3165.

[2] a) X. Li, X. Huang, S. Xi, S. Miao, J. Ding, W. Cai, S. Liu, X. Yang, H. Yang, J. Gao, J. Wang, Y. Huang, T. Zhang, B. Liu, *J. Am. Chem. Soc.* **2018**, *140*, 12469; b) X. Mi, P. Wang, S. Xu, L. Su, H. Zhong, H. Wang, Y. Li, S. Zhan, *Angew. Chem., Int. Ed.* **2020**, *133*, 4638.

[3] a) C. Chu, J. Yang, X. Zhou, D. Huang, H. Qi, S. Weon, J. Li, M. Elimelech, A. Wang, J. H. Kim, *Environ. Sci. Technol.* **2021**, *55*, 1242; b) X. Wu, K. Rigby, D. Huang, T. Hedtke, X. Wang, M. W. Chung, S. Weon, E. Stavitski, J. H. Kim, *Environ. Sci. Technol.* **2022**, *56*, 1341; c) H. Song, R. Du, Y. Wang, D. Zu, R. Zhou, Y. Cai, F. Wang, Z. Li, Y. Shen, C. Li, *Appl. Catal., B* **2021**, *286*, 119898.

[4] K. Qian, H. Chen, W. Li, Z. Ao, Y. Wu, X. Guan, *Environ. Sci. Technol.* **2021**, *55*, 7034.

[5] a) A. Ali, W. Akram, H. Y. Liu, *Molecules* **2019**, *24*, 78; b) J. Jiang, Z. Zhao, J. Gao, T. Li, M. Li, D. Zhou, S. Dong, *Environ. Sci. Technol.* **2022**, *56*, 5611; c) B. Liu, W. Guo, W. Jia, H. Wang, Q. Si, Q. Zhao, H. Luo, J. Jiang, N. Ren, *Environ. Sci. Technol.* **2021**, *55*, 12640.

[6] Y. Zong, X. Guan, J. Xu, Y. Feng, Y. Mao, L. Xu, H. Chu, D. Wu, *Environ. Sci. Technol.* **2020**, *54*, 16231.

[7] J. D. Yang, P. Ji, X. S. Xue, J. P. Cheng, *J. Am. Chem. Soc.* **2018**, *140*, 8611.

[8] a) F. Chen, L. L. Liu, J. J. Chen, W. W. Li, Y. P. Chen, Y. J. Zhang, J. H. Wu, S. C. Mei, Q. Yang, H. Q. Yu, *Water Res.* **2021**, *191*, 116799; b) N. Jiang, H. Xu, L. Wang, J. Jiang, T. Zhang, *Environ. Sci. Technol.* **2020**, *54*, 14057; c) X. Zhou, M. K. Ke, G. X. Huang, C. Chen, W. Chen, K. Liang, Y. Qu, J. Yang, Y. Wang, F. Li, H. Q. Yu, Y. Wu, *Proc. Natl. Acad. Sci. USA* **2022**, *119*, 2119492119; d) F. Li, Z. Lu, T. Li, P. Zhang, C. Hu, *Environ. Sci. Technol.* **2022**, *56*, 8765; e) Y. Xiong, H. Li, C. Liu, L. Zheng, C. Liu, J. O. Wang, S. Liu, Y. Han, L. Gu, J. Qian, D. Wang, *Adv. Mater.* **2022**, *34*, 2110653; f) Y. Li, T. Yang, S. Qiu, W. Lin, J. Yan, S. Fan, Q. Zhou, *Chem. Eng. J.* **2020**, *389*, 124382; g) Z. Zhou, M. Li, C. Kuai, Y. Zhang, V. F. Smith, F. Lin, A. Aiello, D. P. Durkin, H. Chen, D. Shuai, *J. Hazard. Mater.* **2021**, *418*, 126294; h) B. Zhang, X.

Li, K. Akiyama, P. A. Bingham, S. Kubuki, *Environ. Sci. Technol.* **2022**, *56*, 1321; i) L. Peng, X. Duan, Y. Shang, B. Gao, X. Xu, *Appl. Catal., B* **2021**, *287*, 119963; j) F. Chen, L. L. Liu, J. H. Wu, X. H. Rui, J. J. Chen, Y. Yu, *Adv. Mater.* **2022**, *34*, 2202891.

[9] R. Tyburski, T. Liu, S. D. Glover, L. Hammarström, *J. Am. Chem. Soc.* **2021**, *143*, 560.

[10] E. C. Gentry, R. R. Knowles, *Acc. Chem. Res.* **2016**, *49*, 1546.

[11] I. Majerz, *Helv. Chim. Acta* **2016**, *99*, 286.

[12] F. Tong, X. Liang, M. Liu, Z. Wang, Y. Liu, P. Wang, H. Cheng, Y. Dai, Z. Zheng, B. Huang, *ACS Catal.* **2022**, *12*, 3558.

[13] M. Fan, J. Cui, J. Wu, R. Vajtai, D. Sun, P. M. Ajayan, *Small* **2020**, *16*, 1906782.

[14] M. Ha, D. Y. Kim, M. Umer, V. Gladkikh, C. W. Myung, K. S. Kim, *Energy Environ. Sci.* **2021**, *14*, 3455.

[15] a) X. Liu, L. Zheng, C. Han, H. Zong, G. Yang, S. Lin, A. Kumar, A. R. Jadhav, N. Q. Tran, Y. Hwang, J. Lee, S. Vasimalla, Z. Chen, S. Kim, H. Lee, *Adv. Funct. Mater.* **2021**, *31*, 2100547; b) X. X. Wang, D. A. Cullen, Y. T. Pan, S. Hwang, M. Wang, Z. Feng, J. Wang, M. H. Engelhard, H. Zhang, Y. He, Y. Shao, D. Su, K. L. More, J. S. Spendelow, G. Wu, *Adv. Mater.* **2018**, *30*, 1706758.

[16] a) D. Zhao, K. Sun, W. C. Cheong, L. Zheng, C. Zhang, S. Liu, X. Cao, K. Wu, Y. Pan, Z. Zhuang, B. Hu, D. Wang, Q. Peng, C. Chen, Y. Li, *Angew. Chem., Int. Ed.* **2020**, *59*, 8982; b) H. Shang, X. Zhou, J. Dong, A. Li, X. Zhao, Q. Liu, Y. Lin, J. Pei, Z. Li, Z. Jiang, D. Zhou, L. Zheng, Y. Wang, J. Zhou, Z. Yang, R. Cao, R. Sarangi, T. Sun, X. Yang, X. Zheng, W. Yan, Z. Zhuang, J. Li, W. Chen, D. Wang, J. Zhang, Y. Li, *Nat. Commun.* **2020**, *11*, 3049.

[17] Z. Chen, Q. Kang, G. Cao, N. Xu, H. Dai, P. Wang, *Int. J. Hydrogen Energy* **2018**, *43*, 6076.

[18] Y. Min, X. Zhou, J. J. Chen, W. Chen, F. Zhou, Z. Wang, J. Yang, C. Xiong, Y. Wang, F. Li, H. Q. Yu, Y. Wu, *Nat. Commun.* **2021**, *12*, 303.

[19] H. Li, C. Shan, B. Pan, *Environ. Sci. Technol.* **2018**, *52*, 2197.

[20] R. Su, N. Li, Z. Liu, X. Song, W. Liu, B. Gao, W. Zhou, Q. Yue, Q. Li, *Environ. Sci. Technol.* **2023**, *57*, 1882.

[21] Y. Wang, T. Zhou, K. Jiang, P. Da, Z. Peng, J. Tang, B. Kong, W. B. Cai, Z. Yang, G. Zheng, *Adv. Energy Mater.* **2014**, *4*, 1400696.

[22] a) F. Xiao, Z. Wang, J. Fan, T. Majima, H. Zhao, G. Zhao, *Angew. Chem., Int. Ed.* **2021**, *60*, 10375; b) A. Mehmood, M. Gong, F. Jaouen, A. Roy, A. Zitolo, A. Khan, M. T. Sougrati, M. Primbs, A. M. Bonastre, D. Fongalland, G. Drazic, P. Strasser, A. Kucernak, *Nat. Catal.* **2022**, *5*, 311; c) D. Strmcnik, M. Uchimura, C. Wang, R. Subbaraman, N. Danilovic, D. Vliet, A. P. Paulikas, V. R. Stamenkovic, N. M. Markovic, *Nat. Chem.* **2013**, *5*, 300.

[23] N. Yao, G. Wang, H. Jia, J. Yin, H. Cong, S. Chen, W. Luo, *Angew. Chem., Int. Ed.* **2022**, *61*, 202117178.

[24] L. Yu, G. Zhang, C. Liu, H. Lan, H. Liu, J. Qu, *ACS Catal.* **2018**, *8*, 1090.

[25] a) J. Fan, Z. Zhao, Z. Ding, J. Liu, *RSC Adv.* **2018**, *8*, 7269; b) T. Akbarpoor, A. Khazaei, J. Y. Seyf, N. Sarmasti, M. M. Gilan, *Res. Chem. Intermediat.* **2019**, *46*, 1539.

[26] H. Li, Z. Zhao, J. Qian, B. Pan, *Environ. Sci. Technol.* **2021**, *55*, 6397.

[27] A. Al-Riyahee, A. Shenta, K. Saud, *Egypt. J. Chem.* **2021**, *64*, 6337.

[28] C. Zhao, B. Liu, X. Li, K. Zhu, R. Hu, Z. Ao, J. Wang, *Chem. Commun.* **2019**, *55*, 7151.

[29] J. R. Kitchin, J. K. Nørskov, M. A. Barteau, J. G. Chen, *J. Chem. Phys.* **2004**, *120*, 10240.

[30] L. Jiao, L. Xu, Y. Zhang, Y. Wu, W. Gu, X. Ge, B. Chen, C. Zhu, S. Guo, *Nano Today* **2020**, *35*, 100971.